# Incorporating Uncertainty in Admissible Regions for Uncorrelated Detections

Johnny L. Worthy III*, Marcus J. Holzinger†
*Georgia Institute of Technology, Atlanta, GA, 30332*

**Admissible region methods for initial orbit determination are generally implemented without considering uncertainty in observations or observer state. In this paper a generalization of the admissible region approach is introduced that more accurately accounts for uncertainty in the constraint hypothesis parameters used to generate the admissible region. Considering the uncertainty to have Gaussian distributions, the proposed relationship between provided information uncertainty and admissible region uncertainty results directly in an analytical approximate probability density function. The methodology is extended to account for admissible regions with multiple overlapping constraint hypothesis. The proposed approach is applied to an example optical detection to demonstrate the quality of the approximation and the sensitivity of the resulting distribution to typical errors.**

## I. Introduction

For initial detections in dynamical systems there often exist many states that are consistent with the observation, admitting a continuum of candidate state hypotheses. This problem is directly relevant to Space Situational Awareness (SSA) activities as the sensors used to track objects cannot fully measure the state of the object with a single detection. The primary motivation for improving SSA capabilities is to ensure the safety of assets in space, and also to maintain accurate knowledge of the objects orbiting Earth [1]. Over 17,000 objects greater than 10 cm are tracked of which approximately 16,000 are classified as debris from the breakup of known space objects [2]. The Space Surveillance Network (SSN) is the main contributor to maintaining information on detected objects, with a network of optical and radar sensors on both space-based and ground-based observation platforms [3]. Beyond low Earth orbit (LEO), radar observations can be infeasible due to high altitudes, requiring the use of optical sensors. However, altitudes above LEO are very important to SSA as they are valuable for communication and navigation [4].

Optical sensors measure state information as either a series of angle measurements over time or from streaks formed during a single observation. These angular measurements form a tracklet, but the range to the object and the rate at which the range is changing are not directly observable. Thus, the space object state is underdetermined and for a given tracklet a continuum of range and range-rate solutions are possible. However, using Gauss' or Lambert's method an initial orbit determination is possible from three or more angle measurements [5]. The curvature of the orbit appears as a divisor in this approach, thus, the greater the time between observations, the better the estimate. As the time between observations shortens, the quality of the orbit determination degrades greatly. When tracking space objects, telescopes are typically capable of detecting objects for durations on the order of minutes (at most tens of minutes for LEO objects) [6]. At these time scales, traditional initial orbit determination methods (such as Gauss's) fail. Similarly, both radar and magnetometer based observations are susceptible to this problem [7] [8].

This lack of conclusive information at the moment of detection is the motivation of the Too Short Arc (TSA) problem in initial orbit determination of optical tracklets [7] [9]. Because given a TSA the initial orbit determination is poorly posed, a continuum of solutions exist for a particular TSA. However, possible solutions can be bounded under the hypothesis that specified conditions are satisfied. The Admissible Region method first proposed by Milani et. al. accomplishes this and is applied to the problem of constraining the infinite solution space by the dynamics of orbiting bodies [7] [10] [11] [12]. The admissible region method functions by forming hypotheses that the object satisfies a set of physical constraints (e.g., Earth orbiting). Under the assumption that these hypotheses are true, the admissible region may be represented by a uniform probability density function (PDF) in the undetermined state space over the closed, compact set [13]. The resulting PDF is necessarily uniform because there is no additional information available regarding the space object state.

Bayesian estimation requires an $a-priori$ probability distribution of the initial state, necessitating that the admissible region be expressed in a probabilistic manner. Generally, existing admissible region methods discretize the admissible region and consider the solutions at discrete points [14] [15]. A multiple hypothesis filter or particle filter

*Graduate Researcher, School of Aerospace Engineering, and AIAA Student Member.
†Assistant Professor, School of Aerospace Engineering, and AIAA Senior Member.

approach can also be initialized from a discretized admissible region approach and ingest new correlated measurements as they become available [16]. A Gaussian mixture model may be used to approximate the admissible region resulting in a PDF without a discontinuity at the constraint [17]. This Gaussian mixture approach is a convenient method to express the admissible region enabling the use of Gaussian mixture ensemble filters. The main limitation of current initial PDF approximation approaches is that they do not account for the measurement uncertainty of the observer or uncertainty in assumed parameters. Neither the fully uniform distribution nor the Gaussian mixture approaches correctly incorporate the uncertainty inherent to the system. Uncertainties arise from sensor accuracy, timing accuracy, and observer state (i.e. position and velocity) knowledge. Each of these sources of uncertainty are unaccounted for in current methods, making them vulnerable to missing data associations, incorrectly associating data, incorrectly estimating space object orbits, or slower estimation convergence. Weisman et. al. addresses the problem of uncertainty by using a transformation of variables technique to map measurement uncertainties to state uncertainties [18]. However, the transformation of variables technique does not account for uncertainty directly in the admissible region, but rather the uncertainty about a specific point solution.

The admissible region method may also be applied to the association of measurements. It is a fact that, in general, two admissible regions generated from observations that represent different objects do not intersect based on the Theory of Superposition [19]. Thus, multiple admissible regions can be propagated to a common epoch and, if the observations are associated, there will be one point where this intersection occurs [11]. Fujimoto's work shows that the intersection of two associated measurements is an ideal reference orbit for statistical orbit determination methods, but does not offer a true initial PDF; rather, it generates a point solution. If the true PDF for each observation can be approximated, then it follows that if the observations are correlated then using Bayes rule the resulting intersection is no longer a single point, but an approximate PDF which can then be used in statistical orbit determination methods.

To address these issues, this paper introduces a generalization of the Admissible Region method that accounts for measurement and assumed parameter uncertainties. The specific contributions are 1) A generalized definition of the admissible region of the undetermined state space for a given measurement model based on hypothesized constraints, 2) A derivation of the relationship between the uncertainty in the admissible region and the measurement errors and parameter uncertainties based on a Taylor series expansion of hypothesized constraints, 3) An analytical approach to generate the initial PDF in the undetermined state space based solely on the measurement errors and parameter uncertainties, enabling statistically rigorous filter initiation from a single observation sequence, 4) An approach to combine PDFs from multiple constraint hypotheses, 5) A probabilistic method based on Fujimoto's approach to compute the joint PDF using two admissible regions from different epochs.

This paper is organized as follows. The theory supporting the method is introduced in Section II and an application of the method in initial orbit determination is presented in Section III. Within Section III, parts A & B introduce angles-only initial orbit determination, part C demonstrates the approach as applied to an optical observation, part D validates the approach, and part E demonstrates the computation of a joint PDF.

# II. Theory

## A. Admissible States

Admissible states approaches are useful in a variety of applications, and thus a general measurement model is used to derive the approach. A general nonlinear measurement model is assumed,

$$\mathbf{y} = \mathbf{h}(\mathbf{x}; \mathbf{k}, t) \tag{1}$$

where $\mathbf{y} \in \mathbb{R}^m$ is the measurement vector, $\mathbf{x} \in \mathbb{R}^n$ is the state, $\mathbf{k} \in \mathbb{R}^l$ is a parameter vector, and $t \in \mathbb{R}$ is the time. In the case of an underdetermined system the number of states that can be observed, or measured, is less than the number of states in the system, giving $m < n$. This is significant because it implies there is no unique solution for $\mathbf{x}$ given $\mathbf{y}$ in Eqn. (1). This signifies that the undetermined states play no role in determining $\mathbf{y}$. This enables a partitioning of the state vector into the observable and undetermined states.

$$\mathbf{x}_u^T = \begin{bmatrix} \mathbf{x}_d^T & \mathbf{x}_u^T \end{bmatrix} \tag{2}$$

Eqn. (1) becomes

$$\mathbf{y} = \mathbf{h}(\mathbf{x}_d, \mathbf{x}_u; \mathbf{k}, t) \tag{3}$$

where $\mathbf{x}_d \in \mathbb{R}^m$ are the determined states, $\mathbf{x}_u \in \mathbb{R}^u$ are the undetermined states, and $u + m = n$. Since it has already been stated that the undetermined states have no impact on $\mathbf{y}$, it follows that Eqn. (3) can be written simply as

$$\mathbf{y} = \mathbf{h}(\mathbf{x}_d; \mathbf{k}, t) \tag{4}$$

This implies that there exists a unique relationship between $\mathbf{x}_d$ and $\mathbf{y}$ given the observation parameters $\mathbf{k}$ and time $t$. Equivalently, there is a one-to-one and onto mapping from $\mathbf{x}_d$ to $\mathbf{y}$, which means that the inverse mapping is guaranteed provide one-to-one and onto mappings from $\mathbf{y}$ to $\mathbf{x}_d$. Thus,

$$\mathbf{x}_d = \mathbf{h}^{-1}(\mathbf{y}; \mathbf{k}, t) \tag{5}$$

To bound the undetermined state solution space, admissible region methods impose a set of state constraint hypotheses $\mathcal{H} = \{\mathcal{H}_1, \cdots, \mathcal{H}_c\}$. Then an admissible region can be constructed from a given constraint $\mathcal{H}_i \in \mathcal{H}$ under the assumption that a given hypothesis $\mathcal{H}_i$ is true. These constraints may result from the dynamics of the system or from physical limitations and can be represented in the following form

$$g_i(\mathbf{x}_d, \mathbf{x}_u; \mathbf{k}, t) \leq 0 \tag{6}$$

Combining with Eqn. (5) yields

$$g_i(\mathbf{h}^{-1}(\mathbf{y}; \mathbf{k}, t), \mathbf{x}_u; \mathbf{k}, t) \leq 0 \tag{7}$$

This constraint is significant because a given observation will result in a continuum of possible solutions for $\mathbf{x}_u$, but Eqn. (7) defines an $n - m$ dimensional continuum of admissible solutions that all generate the observed measurement. This definition requires that the constraint reduces the set of solutions from an infinite continuum to a compact set with an integrable area. In order to formalize this set, $\mathcal{AR}_i \in \mathbb{R}^u$ is defined.

$$\mathcal{AR}_i := \{\mathbf{x}_u \in \mathbb{R}^u \mid g_i(\mathbf{h}^{-1}(\mathbf{y}; \mathbf{k}, t), \mathbf{x}_u; \mathbf{k}, t) \leq 0\} \tag{8}$$

The set of solutions in $\mathcal{AR}_i$ is also known as the admissible region for hypothesis $\mathcal{H}_i$ in the literature [7] [20] [10]. The combined admissible region for all hypotheses $\mathcal{H}$ is then given by

$$\mathcal{AR} = \mathcal{AR}_1 \cap \cdots \cap \mathcal{AR}_i \cap \cdots \cap \mathcal{AR}_c \tag{9}$$

The boundary of $\mathcal{AR}_i$ can be defined by setting the inequality in the set definition to an equality. This represents the constraint as a surface $\mathcal{B}_i \in \mathbb{R}^{u-1}$.

$$\mathcal{B}_i := \{\mathbf{x}_u \in \mathbb{R}^{u-1} \mid g_i(\mathbf{h}^{-1}(\mathbf{y}; \mathbf{k}, t), \mathbf{x}_u; \mathbf{k}, t) = 0\} \tag{10}$$

Notationally, the constraint of set $\mathcal{B}_i$ can be simply defined as a constraint function

$$g_i(\mathbf{h}^{-1}(\mathbf{y}; \mathbf{k}, t), \mathbf{x}_u; \mathbf{k}, t) \equiv \boldsymbol{\kappa}_i(\mathbf{x}_u, \mathbf{y}, \mathbf{k}, t) = 0 \tag{11}$$

which implies that given $\mathbf{y}, \mathbf{k}$ and $t$, satisfying this equation gives the undetermined states $\mathbf{x}_u$ in the set $\mathcal{B}_i$, which is the boundary of $\mathcal{AR}_i$.

In the absence of uncertainty, the volume enclosed by $\mathcal{B}_i$, or equivalently the admissible region $\mathcal{AR}_i$, is represented as a uniform distribution [7]. This admissible region state membership in the notation proposed in this paper is formally stated as

$$\mathbb{P}[(\mathbf{x}_u \in \mathcal{AR}_i)] = \mathbb{P}[(\boldsymbol{\kappa}_i(\mathbf{x}_u, \mathbf{y}, \mathbf{k}, t) \leq 0)] \tag{12}$$

which, without the effects of uncertainty, gives a uniform value for each state satisfying the constraint. Using Eqn. (12) and the following standard definition, the PDF can be determined.

$$f_i[\mathbf{x}_u] = \frac{\mathbb{P}[\mathbf{x}_u \in \mathcal{AR}_i]}{\int_{\mathcal{AR}_i} \mathbb{P}[\mathbf{x}_u \in \mathcal{AR}_i] d\mathbf{x}_u} \tag{13}$$

Because satisfaction of the constraint is binary, $\mathbb{P}[\mathbf{x}_u \in \mathcal{AR}_i]$ takes on values of 0 or 1, yielding uniform distributions.

### B. Uncertainties in the Admissible States

With an expression for the boundary of the admissible region method $\mathcal{B}_i$ defined, the effects of uncertainty can be investigated. The uncertainty is generated by error in the measurement devices as well as uncertainties in the observer's parameters, such as the observer's position or velocity, and timing inaccuracies. A Taylor series expansion of Eqn. (11) allows for the analysis of the effects of uncertainty on the undetermined states. The Taylor series expansion of Eqn. (11) is given by

$$\boldsymbol{\kappa}_i(\mathbf{x}_u + \delta\mathbf{x}_u, \mathbf{y} + \delta\mathbf{y}, \mathbf{k} + \delta\mathbf{k}, t + \delta t) = \boldsymbol{\kappa}_i(\mathrm{x}_u, \mathbf{y}, \mathbf{k}, t) + \frac{\partial \boldsymbol{\kappa}_i}{\partial \mathbf{x}_u}\delta\mathbf{x}_u + \frac{\partial \boldsymbol{\kappa}_i}{\partial \mathbf{y}}\delta\mathbf{y} + \frac{\partial \boldsymbol{\kappa}_i}{\partial \mathbf{k}}\delta\mathbf{k} + \frac{\partial \boldsymbol{\kappa}_i}{\partial t}\delta t + \cdots + \text{H.O.T} \tag{14}$$

Given any variation in the measurement or parameter vectors, the constraint defines the perturbed location of the admissible region boundary and must necessarily be satisfied, requiring

$$\boldsymbol{\kappa}_i(\mathbf{x}_u + \delta\mathbf{x}_u, \mathbf{y} + \delta\mathbf{y}, \mathbf{k} + \delta\mathbf{k}, t + \delta t) = 0 \tag{15}$$

Using Eqn. (15) and assuming that the variations in $\delta\mathbf{y}$, $\delta\mathbf{k}$, and $\delta t$ are sufficiently small, the higher order terms are negligible. The Taylor series simplifies to

$$-\frac{\partial\boldsymbol{\kappa}_i}{\partial\mathbf{x}_u}\delta\mathbf{x}_u = \frac{\partial\boldsymbol{\kappa}_i}{\partial\mathbf{y}}\delta\mathbf{y} + \frac{\partial\boldsymbol{\kappa}_i}{\partial\mathbf{k}}\delta\mathbf{k} + \frac{\partial\boldsymbol{\kappa}_i}{\partial t}\delta t \tag{16}$$

Eqn. (16) only relates a constant variation in $\mathbf{y}$, $\mathbf{k}$, and $t$ to $\mathbf{x}_u$. It does not give information on how random uncertainties and errors in $\mathbf{y}$, $\mathbf{k}$, and $t$ ($\delta\mathbf{y}, \delta\mathbf{k}, \delta\mathbf{t}$) contribute to a resulting distribution of the undetermined states. The first order sensitivity of the undetermined states in Eqn. (16) can be rewritten as a similar equation in terms of random variables $\delta\mathbf{Y}$, $\delta\mathbf{K}$, and $\delta T$ with each random variable belonging to a Gaussian distribution. Thus, combining the errors $\delta\mathbf{Y}$, $\delta\mathbf{K}$, and $\delta T$ into a single variable $\delta\mathbf{Z} \in \mathbb{R}^{m+l+1}$, Eqn. (16) can be rewritten as

$$-\frac{\partial\boldsymbol{\kappa}_i}{\partial\mathbf{x}_u}\delta\mathbf{X}_u = \frac{\partial\boldsymbol{\kappa}_i}{\partial\mathbf{z}}\delta\mathbf{Z} \tag{17}$$

where $\delta\mathbf{X}_u$ is now a random variable, and the uncertainty distributions in $\delta\mathbf{Z} = \begin{bmatrix}\delta\mathbf{Y}^T & \delta\mathbf{K}^T & \delta T\end{bmatrix}^T$ can be written as

$$\delta\mathbf{Z} \sim \mathcal{N}(\mathbf{0}, \mathbf{P}_z) \tag{18}$$

where $\mathbf{P}_z$ is the known covariance matrix of $\delta\mathbf{Z}$. Eqn. (17) as written is a scalar equation, preventing a direct solution for $\delta\mathbf{X}_u$ without the addition of other constraints.

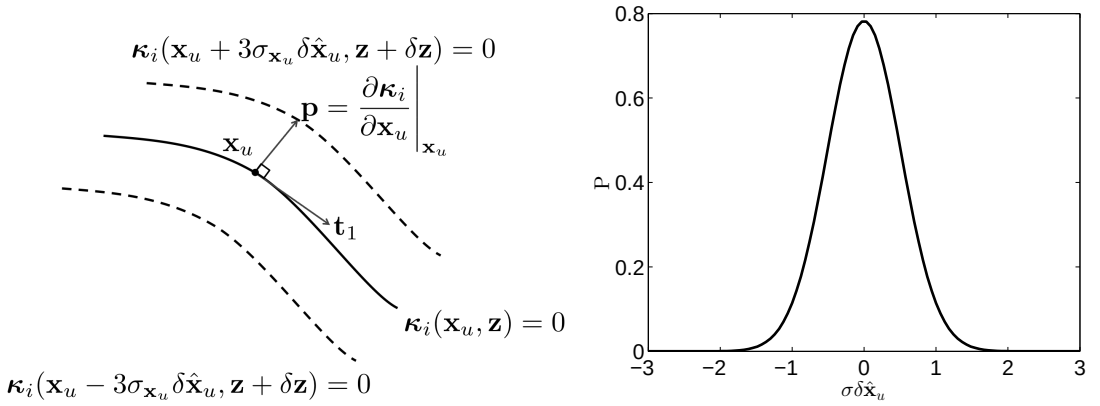


**a) $3\sigma$ Uncertainty bounds for $\boldsymbol{\kappa}_i(\mathbf{x}_u, \mathbf{z})$** **b) Example Gaussian distribution in the $\delta\hat{\mathbf{x}}_u$ direction**

**Figure 1. Determining the constraints for $\delta\mathbf{X}_u$**

Considering the constraint $\boldsymbol{\kappa}_i(\mathbf{x}_u, \mathbf{y}; \mathbf{k}, t)$, the derivative with respect to $\mathbf{x}_u$ will be perpendicular to $\mathcal{B}_i$ at the point $\mathbf{x}_u$. This perpendicular vector is defined as the $\mathbf{p}$ vector

$$\mathbf{p} = \left.\frac{\partial\boldsymbol{\kappa}_i}{\partial\mathbf{x}_u}\right|_{\mathbf{x}_u} \tag{19}$$

With this definition, Eqn. (17) can be rewritten as

$$\mathbf{p}^T\delta\mathbf{X}_u = -\frac{\partial\boldsymbol{\kappa}_i}{\partial\mathbf{z}}\delta\mathbf{Z} \tag{20}$$

Consider the uncertainty $\delta\mathbf{x}_u$ at different locations $\mathbf{x}_u$ along the constraint $\boldsymbol{\kappa}_i$ as shown in Figure 1. The variational location of the boundary can be described by a curve locally parallel to $\boldsymbol{\kappa}_i$, and so at the point $\mathbf{x}_u$, can be fully described by the projection of $\delta\mathbf{x}_u$ in the direction of $\mathbf{p}$. Thus, the solution $\delta\mathbf{x}_u$ should have no component in any tangential directions, enabling the remaining additional constraints to be defined. For an $m$ dimensional measurement, $n-m-1 =$

$u-1$ tangential directions exist. The first tangential direction $\mathbf{t}_1$ is obtained by solving for any vector perpendicular to $\mathbf{p}$. Each subsequent tangential vector in $\mathbb{R}^u$ can be obtained recursively by taking the cross product.

$$\mathbf{t}_j = \mathbf{p} \times \mathbf{t}_{j-1} \text{ for } j = 2, ..., u-1 \tag{21}$$

Thus the matrix of tangential directions is formed by

$$\mathbf{T} = \begin{bmatrix} \mathbf{t}_1^T \\ \vdots \\ \mathbf{t}_{u-1}^T \end{bmatrix} \tag{22}$$

where $\mathbf{T} \in \mathbb{R}^{u-1 \times u}$. To ensure a particular solution of $\delta\mathbf{x}_u$ has no tangential component, the following is defined.

$$\mathbf{t}_i^T \delta\mathbf{X}_u = 0 \tag{23}$$

Combined, the constraints on the solution for $\delta\mathbf{x}_u$ can be written as

$$\begin{bmatrix} \mathbf{p}^T \\ \mathbf{t}_1^T \\ \vdots \\ \mathbf{t}_{u-1}^T \end{bmatrix} \delta\mathbf{X}_u = \begin{bmatrix} \mathbf{p}^T \\ \mathbf{T} \end{bmatrix} \delta\mathbf{X}_u = \begin{bmatrix} -\frac{\partial \boldsymbol{\kappa}_i}{\partial \mathbf{z}_k} \\ \mathbf{0} \end{bmatrix} \delta\mathbf{Z} \tag{24}$$

Because each row and column of the matrix on the left hand side are mutually orthogonal, it is by definition full rank and always invertible, yielding

$$\delta\mathbf{X}_u = \begin{bmatrix} \mathbf{p}^T \\ \mathbf{T} \end{bmatrix}^{-1} \begin{bmatrix} -\frac{\partial \boldsymbol{\kappa}_i}{\partial \mathbf{z}_k} \\ \mathbf{0} \end{bmatrix} \delta\mathbf{Z} \tag{25}$$

This equation expresses the relationship between uncertainties in $\mathbf{z}$ and $\mathbf{x}_u$ such that $\delta\mathbf{X}_u$ is orthogonal to the constraint boundary $\mathcal{B}_i$. Let

$$\mathbf{M}_i = \begin{bmatrix} \mathbf{p}^T \\ \mathbf{T} \end{bmatrix}^{-1} \begin{bmatrix} -\frac{\partial \boldsymbol{\kappa}_i}{\partial \mathbf{z}_k} \\ \mathbf{0} \end{bmatrix}$$

Then, to first order, the random variable $\delta\mathbf{X}_u$ orthogonal to the constraint surface is linearly related to the parameter random variable $\delta\mathbf{z}$.

$$\delta\mathbf{X}_u = \mathbf{M}\delta\mathbf{Z} \tag{26}$$

Now, the statistics of the uncertain boundary location $\delta\mathbf{X}_u$ must be determined. Since $\delta\mathbf{Z}$ belongs to a Gaussian distribution, the expected value of $\delta\mathbf{X}_u$ can be taken as

$$\begin{aligned} \mathbb{E}[\delta\mathbf{X}_u] &= \mathbb{E}[\mathbf{M}\delta\mathbf{Z}] \\ &= \mathbf{M}\mathbb{E}[\delta\mathbf{Z}] \\ &= \mathbf{0} \end{aligned} \tag{27}$$

indicating $\delta\mathbf{X}_u$ has $\mathbf{0}$ mean, which is as expected since the uncertainties in $\delta\mathbf{Z}$ are assumed to belong to Gaussian distributions with $\mathbf{0}$ mean. The covariance of $\delta\mathbf{X}_u$ is derived as follows

$$\begin{aligned} \mathbf{P}_{\mathbf{x}_u} &= \mathbb{E}\left[(\mathbb{E}[\delta\mathbf{X}_u] - \delta\mathbf{X}_u)(\mathbb{E}[\delta\mathbf{X}_u] - \delta\mathbf{X}_u)\right]^T \\ &= \mathbb{E}[(\delta\mathbf{X}_u)(\delta\mathbf{X}_u)^T] \\ &= \mathbb{E}[\mathbf{M}\delta\mathbf{Z}\delta\mathbf{Z}^T\mathbf{M}^T] \\ &= \mathbf{M}\mathbb{E}[\delta\mathbf{Z}\delta\mathbf{Z}^T]\mathbf{M}^T \end{aligned}$$

By definition $\mathbb{E}[\delta\mathbf{Z}\delta\mathbf{Z}^T] = \mathbf{P}_z$ is the variance of $\delta\mathbf{Z}$ which allows

$$\mathbf{P}_{\mathbf{x}_u} = \mathbf{M}\mathbf{P}_{\mathbf{z}}^T\mathbf{M}^T \tag{28}$$

Where $\mathbf{P}_{\mathbf{x}_u} \in \mathbb{R}^{u\times u}$ is the covariance matrix for $\delta\mathbf{X}_u$ at a given point in $\mathcal{B}_i$. Because the relationship between $\delta\mathbf{x}_u$ is linear, if $\delta\mathbf{z}$ is assumed Gaussian then $\delta\mathbf{X}_u$ has no higher moments. Thus, with Equation (28), the distribution of the undetermined states in the direction of $\mathbf{p}$ can be directly analytically approximated from knowledge of the distribution of the uncertainties in $\delta\mathbf{Z}$ at each point on the set $\mathcal{B}_i$ of the admissible region $\mathcal{R}_i$. Furthermore, the Gaussian cumulative distribution function giving $\mathbb{P}[(x \leq X)]$ is fully defined by mean and variance, so the probability that a given $\mathbf{x}_u$ is in the admissible region $\mathcal{R}_i$ can be defined analytically as

$$\mathbb{P}[(\mathbf{x}_u \in \mathcal{R}_i)] = \frac{1}{2}\left[1 + \text{erf}\left(\frac{\|\mathbf{x}_\text{u} - \mathbf{x}_{\text{u},\mathcal{B}_\perp}\|}{\sqrt{2\text{tr}\mathbf{P}_{\mathbf{x}_{\text{u},\mathcal{B}_\perp}}}}\right)\right] \tag{29}$$

where $\mathbf{x}_{u,\mathcal{B}_\perp}$ is the point on the set $\mathcal{B}_i$ that is perpendicular to $\mathbf{x}_u$ and $\mathbf{P}_{\mathbf{x}_{u,\mathcal{B}_\perp}}$ is the covariance matrix computed for that point. The approximate analytical PDF can be fully obtained using Eqn. (29). This particular formulation gives an analytical approach to determine the probability that a given solution $\mathbf{x}_u$ is in the set $\mathcal{R}_i$. Also, note that $\mathbf{x}_d$ is by construction Gaussian ($\mathbf{x}_d \sim \mathcal{N}(\mathbf{x}_d, \mathbf{P}_d)$), so a complete distribution for $\mathbf{x}$ is found. This fundamental result allows for full state uncertainty initialization for an underdetermined detection.

### C. Joint PDF for Multiple Constraints

Given the set of constraints $\mathcal{H}$, it is likely that the PDF of each individual constraint hypothesis $\mathcal{H}_i$ overlaps with those of the other constraints in $\mathbb{R}^u$. The interaction of these PDFs is of interest since the combined PDF provides a full joint distribution under the assumption that all constraint hypotheses are true. To characterize the joint probability, the PDF for a single constraint can be written as

$$f(\mathbf{x}_u \in \mathcal{R}_i) = \frac{\mathbb{P}[\boldsymbol{\kappa}_i(\mathbf{x}_u) \leq 0]}{\int_{\mathcal{R}_i}\mathbb{P}[\boldsymbol{\kappa}_i(\mathbf{x}_u) \leq 0]d\mathbf{x}_u} \tag{30}$$

which can otherwise be written as

$$p(\mathbf{x}_u \in \mathcal{R}_i) = \frac{\mathbb{P}[\boldsymbol{\kappa}_i(\mathbf{x}_u) < 0]}{\int_{\mathcal{R}_i}\mathbb{P}[\boldsymbol{\kappa}_i(\mathbf{x}_u) < 0]d\mathbf{x}_u} \cup \frac{\mathbb{P}[\boldsymbol{\kappa}_i(\mathbf{x}_u) = 0]}{\int_{\mathcal{R}_i}\mathbb{P}[\boldsymbol{\kappa}_i(\mathbf{x}_u) = 0]d\mathbf{x}_u} \tag{31}$$

Furthermore, since $\mathbb{P}[\boldsymbol{\kappa}_i(\mathbf{x}_u) < 0]$ and $\mathbb{P}[\boldsymbol{\kappa}_i(\mathbf{x}_u) = 0]$ are mutually exclusive events

$$p(\mathbf{x}_u \in \mathcal{R}_i) = \frac{\mathbb{P}[\boldsymbol{\kappa}_i(\mathbf{x}_u) < 0]}{\int_{\mathcal{R}_i}\mathbb{P}[\boldsymbol{\kappa}_i(\mathbf{x}_u) < 0]d\mathbf{x}_u} + \frac{\mathbb{P}[\boldsymbol{\kappa}_i(\mathbf{x}_u) = 0]}{\int_{\mathcal{R}_i}\mathbb{P}[\boldsymbol{\kappa}_i(\mathbf{x}_u) = 0]d\mathbf{x}_u} \tag{32}$$

Define $\mathbb{P}[\mathbf{x}_u \in \mathcal{R}]$ as the joint probability that $\kappa_i(\mathbf{x}_u) \leq 0$ for $i = 1, ..., c$ such that

$$\mathbb{P}[\mathbf{x}_u \in \mathcal{R}] = \mathbb{P}[\boldsymbol{\kappa}_1(\mathbf{x}_u) \leq 0] \cap \cdots \cap \mathbb{P}[\boldsymbol{\kappa}_i(\mathbf{x}_u) \leq 0] \cap \cdots \cap \mathbb{P}[\boldsymbol{\kappa}_c(\mathbf{x}_u) \leq 0] \tag{33}$$

Substituting Eqn. (32)

$$\begin{aligned}\mathbb{P}[\mathbf{x}_u \in \mathcal{R}] = &\{\mathbb{P}[\boldsymbol{\kappa}_1(\mathbf{x}_u) < 0] + \mathbb{P}[\boldsymbol{\kappa}_1(\mathbf{x}_u) = 0]\} \cap \cdots \\ &\cap \{\mathbb{P}[\boldsymbol{\kappa}_i(\mathbf{x}_u) < 0] + \mathbb{P}[\boldsymbol{\kappa}_i(\mathbf{x}_u) = 0]\} \cap \cdots \\ &\cap \{\mathbb{P}[\boldsymbol{\kappa}_c(\mathbf{x}_u) < 0] + \mathbb{P}[\boldsymbol{\kappa}_c(\mathbf{x}_u) = 0]\}\end{aligned}$$

This equation simplifies after distributing such that

$$\begin{aligned}\mathbb{P}[\mathbf{x}_u \in \mathcal{R}] = &\{\mathbb{P}[\boldsymbol{\kappa}_1(\mathbf{x}_u) < 0] \cap \cdots \cap \mathbb{P}[\boldsymbol{\kappa}_i(\mathbf{x}_u) < 0] \cap \cdots \cap \mathbb{P}[\boldsymbol{\kappa}_c(\mathbf{x}_u) < 0]\} + \cdots \\ &+ \{\mathbb{P}[(\boldsymbol{\kappa}_1(\mathbf{x}_u) < 0] \cap \cdots \cap \mathbb{P}[\boldsymbol{\kappa}_i(\mathbf{x}_u) = 0] \cap \cdots \cap \mathbb{P}[\boldsymbol{\kappa}_c(\mathbf{x}_u) < 0]\} + \cdots \\ &+ \{\mathbb{P}[\boldsymbol{\kappa}_1(\mathbf{x}_u) = 0] \cap \cdots \cap \mathbb{P}[\boldsymbol{\kappa}_i(\mathbf{x}_u) = 0] \cap \cdots \cap \mathbb{P}[\boldsymbol{\kappa}_c(\mathbf{x}_u) = 0]\}\end{aligned} \tag{34}$$

However, since the distribution of $\delta\mathbf{X}_u$ along the $\mathbf{p}$ direction is a continuous Gaussian distribution, by definition

$$\mathbb{P}[\boldsymbol{\kappa}_i(\mathbf{x}_u) = 0] = 0 \tag{35}$$

This is further demonstrated by examining the rule $\mathbb{P}[A \cap B] = \mathbb{P}[A] + \mathbb{P}[B] - \mathbb{P}[A \cup B]$ and applying it to the $i^{\text{th}}$ constraint.

$$\begin{aligned}\mathbb{P}[(\boldsymbol{\kappa}_i(\mathbf{x}_u) < 0 \cap (\boldsymbol{\kappa}_i(\mathbf{x}_u) = 0))] &= \mathbb{P}[\boldsymbol{\kappa}_i(\mathbf{x}_u) < 0] + \mathbb{P}[\boldsymbol{\kappa}_i(\mathbf{x}_u) = 0] - \mathbb{P}[(\boldsymbol{\kappa}_1(\mathbf{x}_u) < 0) \cup (\boldsymbol{\kappa}_i(\mathbf{x}_u) = 0)] \\ &= \mathbb{P}[\boldsymbol{\kappa}_i(\mathbf{x}_u) < 0] + 0 - \mathbb{P}[(\boldsymbol{\kappa}_i(\mathbf{x}_u) < 0)] \\ &= 0\end{aligned}$$

All of the cross terms in Eqn. (34) vanish leaving

$$\mathbb{P}[\mathbf{x}_u \in \mathcal{AR}] = \mathbb{P}[\boldsymbol{\kappa}_1(\mathbf{x}_u) < 0] \cap \cdots \cap \mathbb{P}[\boldsymbol{\kappa}_i(\mathbf{x}_u) < 0] \cap \cdots \cap \mathbb{P}[\boldsymbol{\kappa}_c(\mathbf{x}_u) < 0] \tag{36}$$

For independent events $A$ and $B$, Bayes' Theorem simplifies as follows

$$\mathbb{P}(A \cap B) = \mathbb{P}(A)\mathbb{P}(B)$$

Under the assumption that the constraints are independent, the probability that $\mathbf{x}_u$ is in the set joint set $\mathcal{AR}$.

$$\mathbb{P}[\mathbf{x}_u] = \mathbb{P}[\boldsymbol{\kappa}_1(\mathbf{x}_u) < 0] \times \cdots \times \mathbb{P}[\boldsymbol{\kappa}_i(\mathbf{x}_u) < 0] \times \cdots \times \mathbb{P}[\boldsymbol{\kappa}_c(\mathbf{x}_u) < 0] \tag{37}$$

were the multiplication is the pointwise multiplication of the probabilities computed for each constraint. Thus, using Eqn. (13), Eqn. (37) and Eqn. (29) the joint PDF for an arbitrary number of constraints can be defined analytically.

Traditional approaches require a discretization of the undetermined state space to generate a joint admissible region probability through Monte Carlo methods. The discretized grid generates a sampling of the state space. For every point in the grid, randomly generated uncertainties are calculated and the constraint function evaluated. Each point in the grid acts as a bin recording the number of times the constraint is met. The probabilities are obtained by dividing the resulting bin values by the total number of trials. The Monte Carlo approach is limited by both the dimensionality of the problem and the resolution of the discretization in addition to long computation times. The analytical approach presented is not limited by dimensionality and doesn't require discretization to generate the joint PDF. Furthermore, the computational requirements for the analytical approach presented are much less than those of Monte Carlo methods.

### D. Track Correlation

The last section presents a method by which several constraints can be combined to generate a joint probability distribution. Similarly, this method can be used to joint probability distributions from different epochs. Fujimoto's work shows that observations can be associated by applying Bayes' rule to an admissible region generated from two epochs [11]. A non-zero result indicates the observations are associated. Specifically, if the objects are associated then there is exactly one solution with non-zero probability.

However, due to observation errors and uncertainties, this particular solution does not fully capture the probability that the measurements are associated. It is possible to, through the inclusion of uncertainty, instead obtain a distribution around this point. Consider two admissible region PDFs $f(\mathbf{x}(t_2); \boldsymbol{\kappa}_i(\mathbf{x}_u, \mathbf{z}_1, t_1))$ and $f(\mathbf{x}(t_2); \boldsymbol{\kappa}_j(\mathbf{x}_u, \mathbf{z}_2, t_2))$, where $\mathbf{x}(t_2)$ denotes that the admissible region generated from $\boldsymbol{\kappa}_i(\mathbf{x}_u, \mathbf{z}_k, t_k)$ is propagated to a common time $t_2$. Assuming that each observation is statistically independent, then applying Bayes' rule as before

$$f(\mathbf{x}(t_2); \boldsymbol{\kappa}_i(\mathbf{x}_u, \mathbf{z}_1, t_1)) \cap f(\mathbf{x}(t_2); \boldsymbol{\kappa}_j(\mathbf{x}_u, \mathbf{z}_2, t_2)) = f(\mathbf{x}(t_2); \boldsymbol{\kappa}_i(\mathbf{x}_u, \mathbf{z}_1, t_1)) \times f(\mathbf{x}(t_2); \boldsymbol{\kappa}_j(\mathbf{x}_u, \mathbf{z}_2, t_2)) \tag{38}$$

Eqn. (38) gives the joint probability that a particular state $\mathbf{x}_u$ is in the admissible region at both times. Using Eqn. (13) the joint probability density can then be computed. Importantly, it is not necessary that each measurement result from the same sensor phenomenology, nor is it required that $t_1 \leq t_2$.

### E. Summary

The presented approach is valid for any measurement sensor with undetermined states, such as optical, radar, or magnetometer sensors. Furthermore, any constraint hypothesis that is valid for the system observed may be used with this approach. For SSA, this may include minimum or maximum orbit energy constraints, illumination constraints, inclination constraints, etc. This approach provides a methodology to approximate uncertainty in the admissible states based on the observer and assumed parameter uncertainty. Then, assuming a known Gaussian distribution for the observer's uncertainty $\delta\mathbf{Z}$, the distribution of the admissible region is analytically approximated. This enables a probability distribution function in the admissible region $\mathcal{AR}_i$ to be analytically generated simply by knowing the uncertainties associated with the measurement sensors and observer. This analytical method can generate an approximate distribution several orders of magnitude faster than Monte Carlo numerical analyses, improving computational tractability for practical use. The analytical method is also extended to multiple constraints to generate a combined admissible region $\mathcal{AR}$ and the resulting combined joint PDF associated with $\mathcal{AR}$. The proposed method can also be used for associating admissible regions at different epochs by computing the joint probability distribution formed by each observation.

# III. Application

## A. Angles-Only Initial Orbit Determination

The proposed methodology in the Theory section is applied in this section to the problem of initial orbit determination for space objects using optical measurements. This section begins with a review of the relevant results originally developed by Milani et. al. [7] [20], then applies the theoretical contributions of this paper. Optical measurements generate angle and angle rates of the objects tracked using a streak or sequence of angle measurements in right ascension $\alpha$ and declination $\beta$. The parameters associated with optical measurements include the observer position, $\mathbf{o}$ and velocity, $\dot{\mathbf{o}}$, and the times at which the observations are made (or the start/stop times of a streak). Using this information, the position $\mathbf{r}$ and velocity $\mathbf{v}$ of the object are given by

$$\begin{aligned}\mathbf{r} &= \mathbf{o} + \rho\hat{\mathbf{l}}\\ \mathbf{v} &= \dot{\mathbf{o}} + \dot{\rho}\hat{\mathbf{l}} + \rho\dot{\alpha}\hat{\mathbf{l}}_\alpha + \rho\dot{\beta}\hat{\mathbf{l}}_\beta\end{aligned}$$

where $\alpha$ is the right ascension, $\beta$ is the declination, $\rho$ is the range to the target, $\dot{\rho}$ is the range-rate, and $\hat{\mathbf{l}}$, $\hat{\mathbf{l}}_\alpha$, and $\hat{\mathbf{l}}_\beta$ are given by

$$\hat{\mathbf{l}} = \begin{bmatrix}\cos\alpha\cos\beta\\ \sin\alpha\cos\beta\\ \sin\beta\end{bmatrix}$$

$$\hat{\mathbf{l}}_\alpha = \begin{bmatrix}-\sin\alpha\cos\beta\\ \cos\alpha\cos\beta\\ 0\end{bmatrix}$$

$$\hat{\mathbf{l}}_\beta = \begin{bmatrix}\cos\alpha\sin\beta\\ -\sin\alpha\sin\beta\\ \cos\beta\end{bmatrix}$$

For this system the states $\mathbf{x}$, observations $\mathbf{y}$, and parameters $\mathbf{k}$ are defined as follows.

$$\begin{aligned}\mathbf{x}^T &= \begin{bmatrix}\alpha & \dot{\alpha} & \beta & \dot{\beta} & \rho & \dot{\rho}\end{bmatrix}\\ \mathbf{y}^T &= \begin{bmatrix}\alpha_1 & \cdots & \alpha_q & \beta_1 & \cdots & \beta_q\end{bmatrix}\\ \mathbf{k}^T &= \begin{bmatrix}\mathbf{o}^T & \dot{\mathbf{o}}^T\end{bmatrix}\end{aligned}$$

where $q$ is the number of observations made and $\dot{\alpha}$ and $\dot{\beta}$ are the angle rates.

For an observation with two measurements, the combined measurement and parameter vector $\mathbf{z} \in \mathbb{R}^{12}$ is simply given by

$$\mathbf{z}^T = \begin{bmatrix}\alpha_1 & \alpha_2 & \beta_1 & \beta_2 & t_1 & t_2 & \mathbf{o}^T & \dot{\mathbf{o}}^T\end{bmatrix} \tag{39}$$

To generate the angle rate data from angle pairs in $\mathbf{z}$, a Lagrange Interpolation shown in Eqn. (40) is used. Using this interpolation, the effects of time uncertainty can be accounted for.

$$\begin{aligned}\dot{\alpha} = \alpha(t_1)\frac{(t-t_2)+(t-t_3)+\cdots+(t-t_n)}{(t_1-t_2)(t_1-t_3)\cdots(t_1-t_q)} + \alpha(t_2)\frac{(t-t_2)+(t-t_3)+\cdots+(t-t_q)}{(t_2-t_1)(t_2-t_3)\cdots(t_2-t_q)}\\ +\cdots+\alpha(t_l)\frac{(t-t_1)+(t-t_2)+\cdots+(t-t_{q-1})}{(t_q-t_1)(t_q-t_2)\cdots(t_l-t_{q-1})}\end{aligned} \tag{40}$$

From Eqn. (40) and $\mathbf{y}$, 4 of the 6 states of $\mathbf{x}$ can be observed or determined and the undetermined states for this system are given by

$$\mathbf{x}_u = \begin{bmatrix}\rho\\ \dot{\rho}\end{bmatrix}_{2\times1} \tag{41}$$

## B. Constraints for Initial Orbit Determination

With the undetermined states $\mathbf{x}_u$ defined, constraint hypotheses on those states must be imposed. Many constraints exist for orbiting bodies based on the assumptions made. A primary assumption for simple analyses is that of 2-body motion, allowing for the specific orbital energy equation to be used. The constraint $\boldsymbol{\kappa}_1$ is generated by enforcing the energy equation such that the space object orbits about the Earth. To constrain the solutions to only objects in orbit about Earth, the admissible region set $\mathcal{R}$ can be defined as $\{\mathbf{x}_u \in \mathbb{R}^2 | \varepsilon(\mathbf{r}, \dot{\mathbf{r}}) \leq 0\}$. The set $\mathcal{B}_1$ is then defined as $\{\mathbf{x}_u \in \mathbb{R}^2 | \varepsilon(\mathbf{r}, \dot{\mathbf{r}}) = 0\}$, which is given as the solution to the following equation.

$$\boldsymbol{\kappa}_1(\mathbf{x}_u, \mathbf{y}_p) = 2\varepsilon(\mathbf{r}, \dot{\mathbf{r}}) = \dot{\rho}^2 + w_1\dot{\rho} + w_2\rho^2 + w_3\rho + w_4 - \frac{2\mu}{\sqrt{\rho^2 + w_5\rho + w_0}} = 0 \tag{42}$$

with $w_0$ through $w_5$ defined as in [10].

$$w_0 = \|\mathbf{o}\|^2 \qquad w_3 = 2\dot{\alpha}\left\langle \dot{\mathbf{o}} \cdot \hat{\mathbf{l}}_\alpha \right\rangle + 2\dot{\beta}\left\langle \dot{\mathbf{o}} \cdot \hat{\mathbf{l}}_\beta \right\rangle$$
$$w_1 = 2\left\langle \dot{\mathbf{o}} \cdot \hat{\mathbf{l}} \right\rangle \qquad w_4 = \|\dot{\mathbf{o}}\|^2$$
$$w_2 = \dot{\alpha}^2 \cos^2\beta + \dot{\beta}^2 \qquad w_5 = 2\left\langle \mathbf{o} \cdot \hat{\mathbf{l}} \right\rangle$$

From Eqn. (42) the solution continuum $\mathbf{x}_u$ satisfying the constraint can be determined given $\mathbf{z}$. Also from Eqn. (42) $\mathbf{t}$ and $\mathbf{p}$ directions are defined at each point on $\mathcal{B}_1$ simply as

$$\mathbf{p}(\mathbf{x}_u)^T = \left[\frac{\partial \boldsymbol{\kappa}_1}{\partial \rho} \quad \frac{\partial \boldsymbol{\kappa}_1}{\partial \dot{\rho}}\right]_{\mathbf{x}_u}$$
$$\mathbf{t}(\mathbf{x}_u)^T = \left[-\frac{\partial \boldsymbol{\kappa}_1}{\partial \dot{\rho}} \quad \frac{\partial \boldsymbol{\kappa}_1}{\partial \rho}\right]_{\mathbf{x}_u}$$

With $\boldsymbol{\kappa}_1$ defined, an example deterministic admissible region is computed based on the measurements given in Table 1 and the observer parameters given in Table 2. The admissible region computed from this observation is shown in Figure 2. As can be seen in Figure 2a, without inclusion of measurement uncertainty, the approach generates an uniform distribution with a discontinuous probability density at the boundary.

**Table 1. Optical Observation Measurements**

| Time (UTC) | $\alpha$ (rad) | $\delta$ (rad) |
|---|---|---|
| 02:01:36 | 0.7666 | -0.5988 |
| 02:01:37 | 0.7685 | -0.5995 |
| 02:01:38 | 0.7704 | -0.6001 |

**Table 2. Observer Parameters (Atlanta, GA)**

| | |
|---|---|
| Location (Lat, Lon, Alt) | 33.77°N, 84.39°W, 340m |
| Cartesian Position (km) | $\begin{bmatrix}-1359.0 & 5128.8 & 3527.9\end{bmatrix}$ |

## C. Accounting for Uncertainty

Recall the standard admissible region (shown in Figure 2) has a uniform probability distribution within the constraint. To approximate the true PDF, the uncertainties must be taken into account while computing the admissible region. The measurements and parameters are assumed to have normal distributions with $\mu = 0$ and $\sigma$ defined by the error associated with each quantity. The errors are given below and are consistent with or better than the performance of Raven-class telescopes used for SSA.

As stated, the analytical approach does not require discretization of the state space. However, in order to both visualize and compare the results with a numerical Monte Carlo approach a discretization of the state space is utilized. Since the approach is analytical, the accuracy of the PDF generated is only dependent upon the approximation of the linearization and the resolution of the discretization. For this observation $\rho$ is discretized to 0.0014 $R_e$ resolution and $\dot{\rho}$ is discretized to 0.003 $R_e$/TU giving 250,000 total points. Equation (29) is then evaluated at each point in the grid to generate $\mathbb{P}[\mathbf{x}_u \in \mathcal{R}_1]$, which can then be normalized to compare the approximate PDF. This enables a direct comparison between the numerical and analytical approaches as the discretization grid used by each is identical. Figure

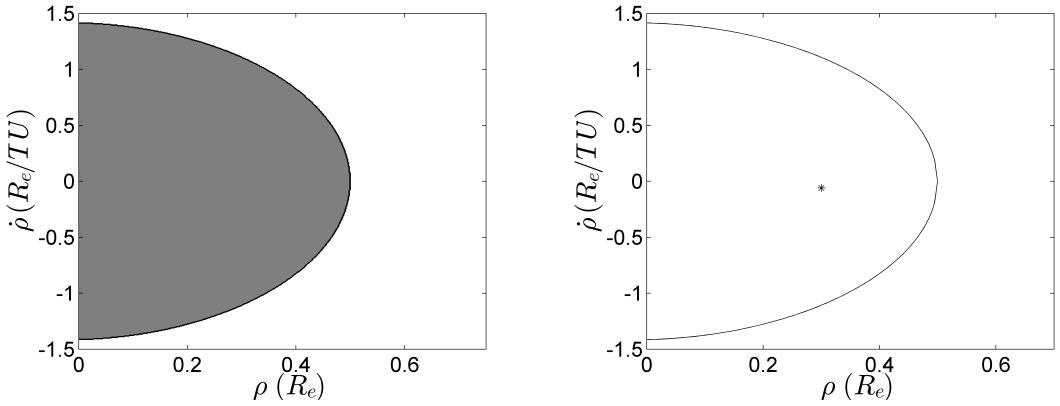


**a) Probability over the undetermined state space for the energy constraint for this observation with no uncertainty effects**

**b) The true state (denoted with the marker) shown along with the boundary $\mathcal{B}_1$ of the admissible region.**

**Figure 2. Admissible region for the example observation**

**Table 3. Measurement Error and Parameter Uncertainty**

| | |
|---|---|
| Right Ascension uncertainty, $\sigma_\alpha$ | 10 arcseconds |
| Declination uncertainty, $\sigma_\beta$ | 10 arcseconds |
| Timing error, $\sigma_t$ | 0.0001 s |
| Position error (each axis), $\sigma_{\mathbf{o}}$ | 1 m |
| Velocity error (each axis), $\sigma_{\dot{\mathbf{o}}}$ | 1 m/s |

4 shows the resulting analytically generated PDF. To visualize the results, Figure 4b shows the $\pm 3\sigma$ bounds of the approximate PDF as well as the nominal constraint curve. This plot shows how significant an effect the measurement uncertainties have on the admissible region. Parts of the state space are unaccounted for without the inclusion of uncertainty, and that, to appropriately use admissible regions, observation uncertainty must be accounted for.

### D. Validation of the Approximation

The analytical approach presented is based on a first order approximation using a Taylor series expansion. Since it is an approximation, error between analytically and numerically obtained results are expected. The purpose of this section is to quantify this error.

#### *1. True PDF*

Figure 3 shows the full PDF with uncertainty calculated from the analytical approximation, but the true PDF can also be computed numerically. Since $\delta\mathbf{Z}$ is given by Eqn. (18) and the measurement and parameter errors are given in Table 3, a Monte Carlo simulation can provide the true distribution in $\delta\mathbf{x}_u$. Since $\delta\mathbf{Z} \in \mathbb{R}^{12}$ for this example application, the Monte Carlo simulation requires a large sample size to sufficiently capture the distribution of the data. A Monte Carlo simulation with one million samples is generated for an identical discretized state space grid as the analytical approximation and each point in the grid is evaluated one million times. To expedite this process, the algorithm was programmed to utilize a Tesla C2050 GPU through the GPU programming functionality in MATLAB. The results from the analysis are shown in Figure 4. Even with the calculations being performed on the GPU, the run time for the Monte Carlo algorithm is approximately 2 hours. In contrast, the analytical PDF is generated in 2 minutes on the same machine (specs listed in Table 4) without GPU processing.

**Table 4. Computer Specs**

| | |
|---|---|
| GPU | Tesla C2050 |
| OS | RHEL 5 |

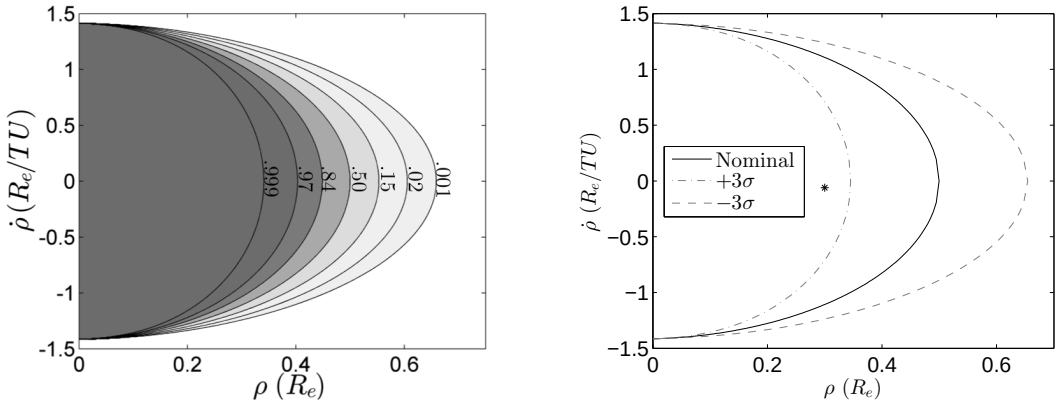


**a) Analytical probability including uncertainties over the undetermined state space**

**b) The $\pm 3\sigma$ bounds for the approximate analytical PDF shown in addition to the nominal boundary. The true state is denoted with the marker**

**Figure 3. PDF for the example observation including measurement uncertainty**

In order to further assess how well the analytical probabilities agrees with the Monte Carlo probabilities, an additional metric is defined in the following section.

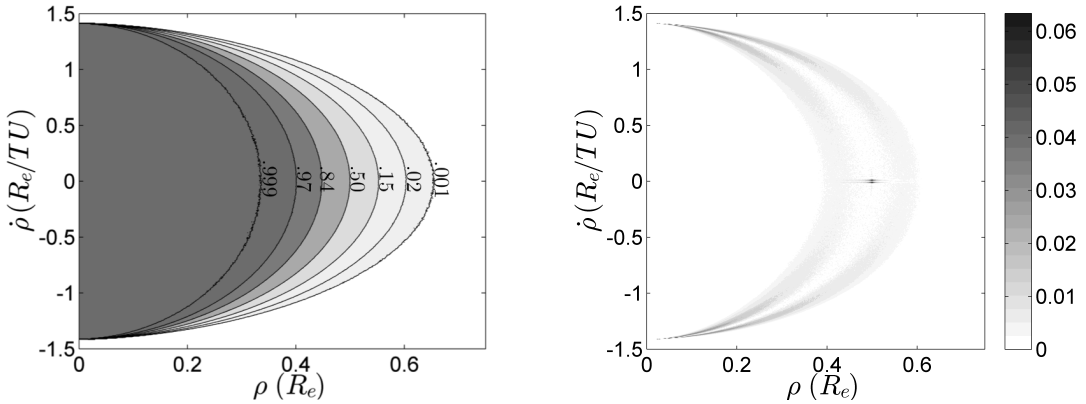


**a) 'True' Monte Carlo numerical probabilities over the undetermined state space**

**b) Error in approximate probabilities relative to Monte Carlo PDF.**

**Figure 4. Monte Carlo simulation results**

### *2. Kullback-Leibler divergence*

The comparison of the analytical and numerical results is fundamentally a comparison of two distributions. Thus, a measure of the similarity of the distributions can be used as a metric of the quality of the analytical approximation. Eqn. (29) defines the probability distribution along the lines normal to the constraint curve, in the expected value case, and both the numerical and analytical solutions should have identical curves for $\sigma = 0$. Equivalently, the analytical and numerical curves (i.e. $\sigma = 0$) without considering uncertainty should be identical. This implies that for this specific case the distribution in the $\mathbf{p}$ direction at identical points on the should also be identical, enabling a comparison of the accuracy of the analytical solution. To define these points a line integral is defined for the $\sigma = 0$ curve such that for each point on the line, the distribution in the $\mathbf{p}$ direction is obtained for both approaches. The line integral along a given constraint curve $\boldsymbol{\kappa}_i$ parameterized by $s \in [0, 1]$ is defined as follows. Defining the $j^{th}$ point in the set of $n$ states

comprising $\mathcal{B}_i$ as $\mathbf{x}_{j,\mathcal{B}_i}$, the total length, $L$, of $\boldsymbol{\kappa}_i$ for $\mathbf{x}_u \in \mathbb{R}^2$ can be defined by

$$L = \sum_{j=1}^{n-1} \|\mathbf{x}_{j+1,\mathcal{B}_i} - \mathbf{x}_{j,\mathcal{B}_i}\|_2 \tag{43}$$

Figure 5 illustrates this for an example admissible region. As shown, $\sum \Delta L$ gives the total length of the admissible

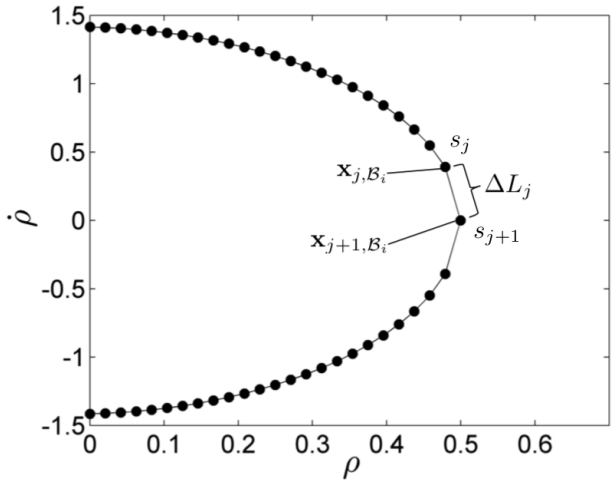


**Figure 5. Two points along L used to calculate $\Delta L_j$**

region curve enabling the line integral $s$ to be defined such that $\Delta s$, along the line $s_i$ can be computed as

$$\begin{aligned}\Delta s_j &= \frac{\Delta L_j}{L} \\ &= \frac{\|\mathbf{x}_{j+1,\mathcal{B}_i} - \mathbf{x}_{j,\mathcal{B}_i}\|_2}{L}\end{aligned}$$

This procedure normalizes the constraint curve to the domain $s \in [0, 1]$ allowing for the analytically and numerically computed uncertainties to be conveniently compared. For the numerically generated PDF the $-3\sigma$ through $3\sigma$ contours are extracted and by generating a line integral for each contour. Then an interpolation through the extracted points can be used to generate the numerical distribution corresponding to each point along $s$. The analytical distributions are fully defined at each point along $s$ with zero mean and variance given by Eqn (28). With both the analytically and numerically computed distributions in the $\mathbf{p}$ direction along $s$ defined, the Kullback-Leibler divergence is utilized to numerically compare the distributions.

The Kullback-Leibler (KL) divergence metric, $D_{KL}$, also known as the information divergence, is a measure of the difference between two probability distributions $P$ and $Q$ [21]. It is a measure of information lost when $Q$ is used to approximate $P$. It should be noted that the KL divergence is not symmetric, implying $D_{KL}$ from $P$ to $Q$ is not the same as from $Q$ to $P$.

$$D_{kl}(P\|Q) = \sum_i \ln\left(\frac{P(i))}{Q(i))}\right) P(i) \tag{44}$$

The equation given above is the form of the KL divergence for discrete probability distributions, where $i$ is an index of the discrete probabilities being compared. Though the probability distributions approximated for the uncertainties are continuous, only discrete points from that distribution are known and thus the approximation of the KL divergence for the numerically and analytically computed distributions as discrete is appropriate.

Because both distributions necessarily have zero mean, quantifying error in the analytical approximation can be accomplished by examining error in the standard deviation. To asses how the values determined for $D_{KL}$ relate to the quality of the approximation, two standard Normal distributions are generated as follows

$$\begin{aligned}P &\sim \mathcal{N}(0, \sigma_P) \\ Q &\sim \mathcal{N}(0, \sigma_P(1 + \%\text{err}))\end{aligned}$$

where $\sigma_{\%errr}$ is the percent error difference from $\sigma_P$. By varying the % error up to 100%, Figure 6 shows how $D_{KL}$ changes for standard normal distributions. Using this plot, an interpolation can be defined to approximate the % error that corresponds to a given $D_{KL}$. The resulting interpolation is then used along with Eqn. (44) such that both % error

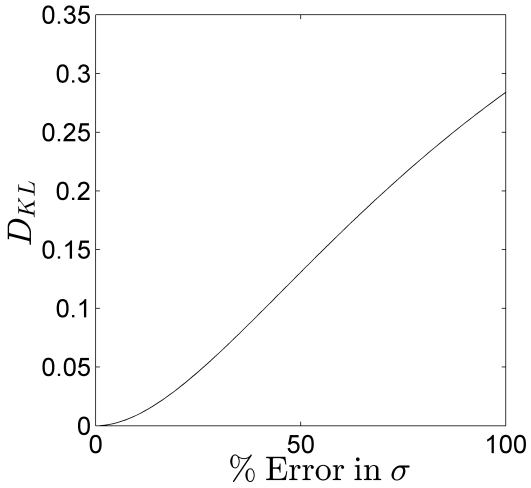


**Figure 6. $D_{KL}$ as a function of % error for a standard Normal distribution**

and $D_{KL}$ can be evaluated. The numerically computed distributions are defined as $Q$ and the analytically computed distributions are defined as $P$. Thus at each point along $s_i$ both $P$ and $Q$ are used to compute $D_{KL}$ and, using the inverse of the relationship shown in Figure 6, the corresponding percent error between the numerical and analytical cases is computed.

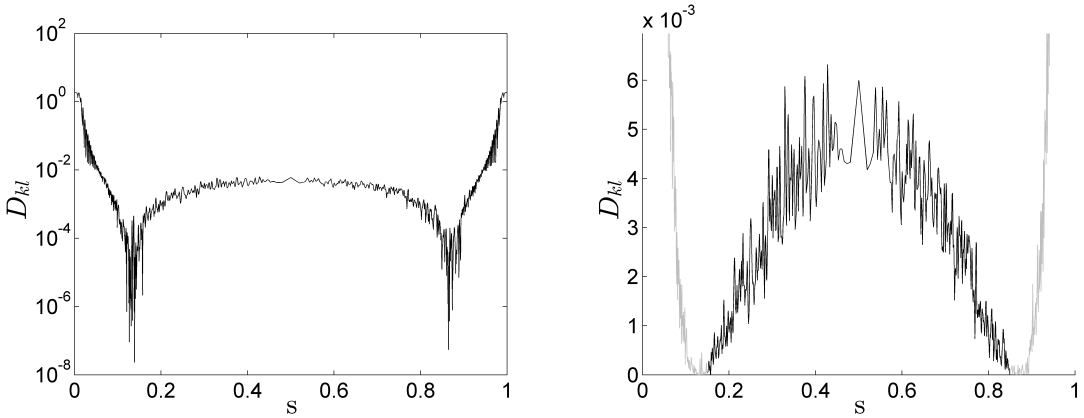


**a) Near the ends of $s$, $D_{KL}$ behaves poorly due to the effects of discretization of the state space.**

**b) Utilizing $s \in 0.25, 0.75$ avoids the effects of discretization**

**Figure 7. Plots of $D_{KL}$ comparing the analytical and Monte Carlo simulation**

Figure 7a shows $D_{KL}$ for the full length of $s$. However, at the ends of the distribution $D_{KL}$ increases substantially. This increase is due to the effects of the discretization as well as the effects of uncertainty. Recalling Figure 4a, as the constraint approaches $\rho = 0$, the distribution narrows. This can be explained probabilistically as the variances computed by Eqn (28) decrease as $\rho \to 0$. As the distribution narrows with a constant, predefined discretization, the width of the distribution becomes too small for the discretization to adequately sample from the distribution. This can be avoided by selecting a discretization size based on the smallest distribution width, however such an approach would be computationally infeasible. Alternatively, a discretization could be selected such that a significant portion of $s$ provides adequate sampling of the probability distribution in that region. Thus, 7b shows $D_{KL}$ for the region of $s \in [0.25, 0.75]$. Over this range, the values of $D_{KL}$ behave as expected implying that over this range of $s$ the discretization is sufficient.

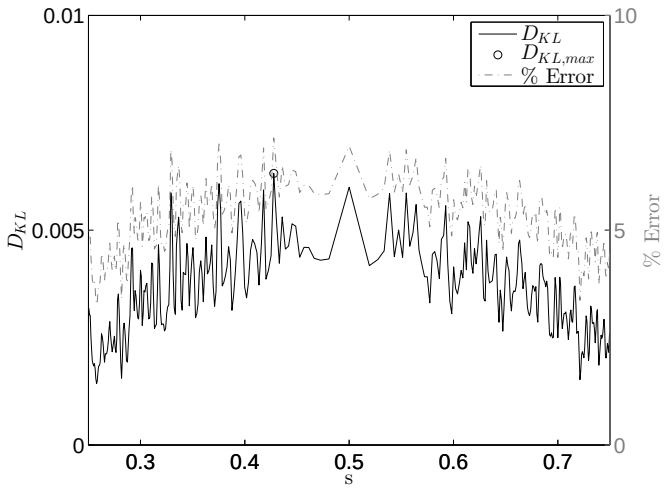


**Figure 8. $D_{KL}$ over the well behaved region of the line $s$ plotted along with % Error. The largest value of $D_{KL}$ occurs at $s = 0.4276$ with 7.15% error.**

Analyzing the results of Figure 8, the greatest Kullback-Leibler divergence is found to be at $s = 0.4276$. This matches with expectation since this problem is derived using a Taylor series approach, thus the largest errors are expected in the high curvature regions of the approximation. The analytically and numerically obtained distribution functions are shown in Figure 9 for $s = 0.4276$. Note that the numerical distributions are fit to the points from the Monte Carlo simulation. It is evident in Figure 9a that the means of the two approaches are well in agreement. This is as expected as the uncertainties belong to a distribution with zero mean. Further, it is shown in Eqn. (27) that the mean of the distribution in the undetermined states should be zero. At this point, the location of the highest error between the approaches, the main difference between the numerical and analytical approaches is the apparent overestimation of the standard deviation from the analytical approach. This is evident due to the narrower peak of the numerical distribution, indicating the true distribution has a lower standard deviation than what is approximated analytically.

Using the inverse of the relationship between $D_{KL}$ and % error shown in Figure 6, Figure 8 plots both $D_{KL}$ and % error on a single axis. The location of the maximum $D_{KL}$ is marked with a circle on the plot and at this point the highest % error of the approach is 7.148%. Overall, the approach shows to be in good agreement with the numerical results. It should be noted that several effects contribute to the accuracy of the analytical approach. The first order approximation used to derive the approach contributes to the errors presented. A numerical method is capable of capturing the higher order effects whereas in the presented analytical approach they are assumed negligible, so a certain amount of error is to be expected. However, it is shown that this error is relatively small and additional factors can contribute to lowering the error. Lower uncertainties will improve the analytical approximation. Additionally, having larger time steps between observations will improve the agreement of the analytical and numerical PDFs reducing error. Uncertainty increases as the time between observations decreases. Larger uncertainties contribute more to the higher order effects neglected in the approach. With longer time steps, uncertainty decreases overall and the error between the numerical and analytical results will decrease as well.

### E. Joint PDF with Two Constraints

Since many underdetermined systems can be subject to several constraint hypotheses, the joint PDF is of much interest. The approach presented in Section II.C for generating a joint PDF is applied to the same observation information $\mathbf{z}$ by considering both an energy constraint as well as a constraint on the periapse radius of the object. For ground observers the periapse radius of the object can be constrained using the following approach [7]. The apparent angular rate of the object with respect to the observer is given by the proper motion $\eta$ where

$$\eta = \sqrt{w_2} \tag{45}$$

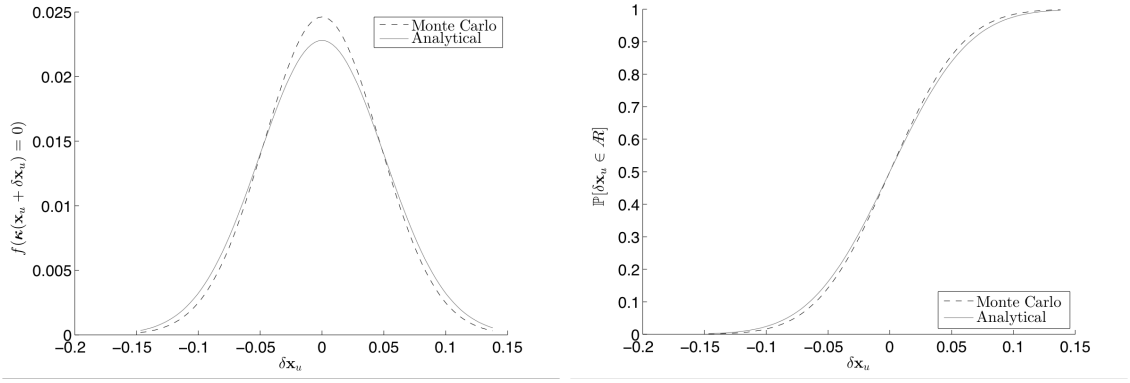


**a) Comparison of the analytical probability distribution with a fit of the Monte Carlo**

**b) Comparison of the cumulative distribution with a fit of the Monte Carlo**

**Figure 9. Validation of the probability and cumulative distribution functions for the numerical and analytical cases at $s = 0.5$ (peak $D_{KL}$ error)**

Thus the range-rate can be equivalently written as $\dot{\rho} = \rho\eta$ and thus it is required that

$$|\dot{\rho}\tau| \geq R_e$$
$$|\rho\eta\tau| \geq R_e$$

where $R_e$ is the radius of the Earth. Additionally, $\tau = \rho/|\dot{\rho}|$ which, after simplification, leaves

$$\frac{\rho^2\eta}{|\dot{\rho}|} \geq R_e$$

which can be written as a quadratic in $\rho$.

$$\frac{R_e|\dot{\rho}|}{\eta} - \rho^2 \leq 0 \tag{46}$$

Eqn. (46) represents the second constraint $\boldsymbol{\kappa}_2(\mathbf{x}_u)$. Following the same procedure as with the energy constraint, the approximate and true Monte Carlo PDFs for $\boldsymbol{\kappa}_1(\mathbf{x}_u)$ and $\boldsymbol{\kappa}_2(\mathbf{x}_u)$ are generated and the joint PDF is computed from the element-wise multiplication of the two distributions. Figure 10 shows the PDF generated for the energy constraint alone. The joint approximate analytic PDF is computed using Eqn. (29) and shown in Figure 11 from the multiplication of the PDF shown in Figure 10 with the PDF from Figure 4. A numerical Monte Carlo joint PDF is generated as well and the results are shown in Figure 12. Figure 13 shows the error between the numerical and analytical joint PDFs by subtracting the two. To generate an additional metric of comparison for the joint PDF, a % error calculation was performed assuming the numerical distribution as the true distribution. Figure 14 shows the computed % error between the analytical PDF shown in Figure 11 and that of Figure 12. Overall, the joint PDF approximated from the analytical approach agrees well with the numerical case. For solutions not in the vicinity of the intersection, the analytical approach almost exactly matches, with less than 5% error in these regions. At the intersections, however, the approximation has up 25% error. For reference, the two admissible region curves are plotted in Figure 13 highlighting the location of the intersection. It is stated previously that one of the contributions to the error in the analytical approach is the first order approximation. Since the product of the individual admissible regions yields the joint PDF, it is expected that the errors of each compounds to give areas of high % error. This is indeed the case for the example observation.

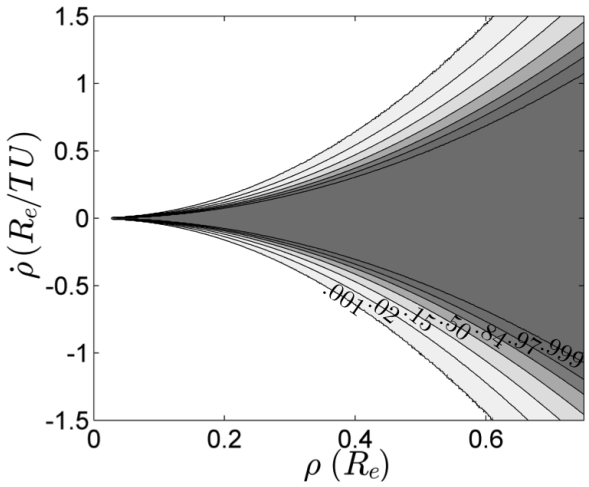


**Figure 10. The probability generated for the periapse constraint alone**

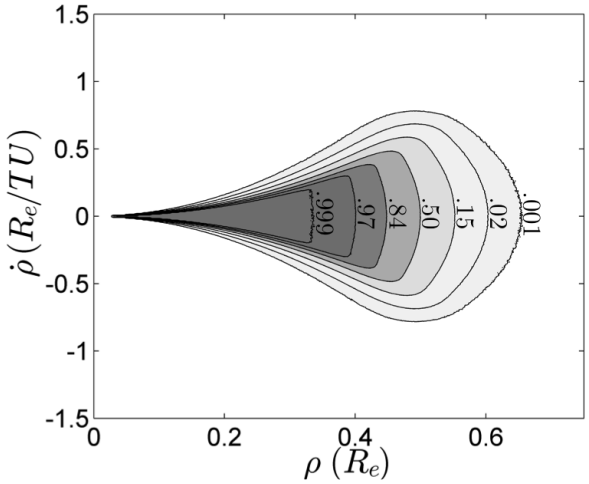


**Figure 11. The joint probability as obtained analytically for the energy and periapse constraints**

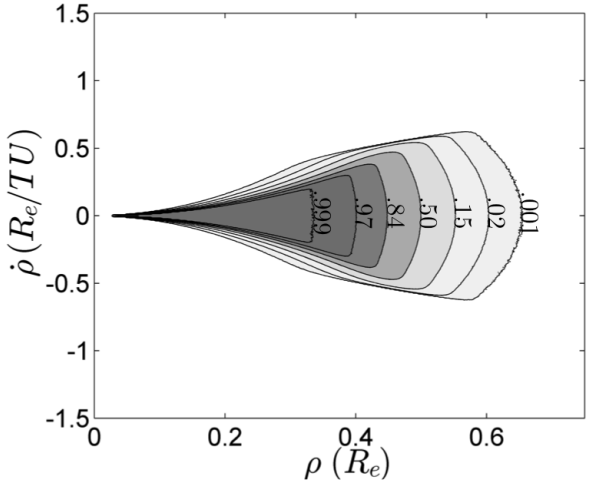


**Figure 12. The joint probabilitiy as obtained from the Monte Carlo simulation for the energy and periapse constraints**

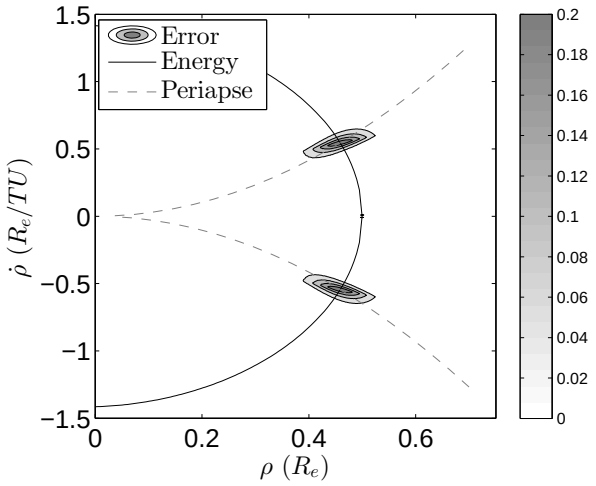


**Figure 13. The difference between the numerically computed joint PDF and the analytically computed joint PDF.**

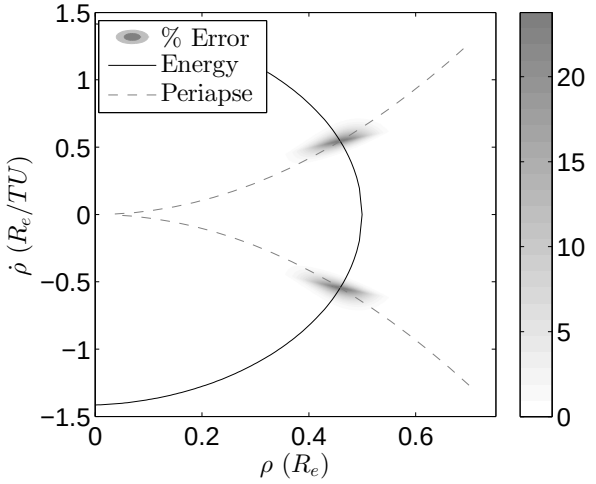


**Figure 14. The percent error between the numerically computed joint PDF and the analytically computed joint PDF.**

## IV. Conclusions & Future Work

This work generalizes the admissible region method for initial orbit determination and presents a method by which measurement and observer uncertainties can be rigorously included in the admissible region. From a general measurement model, the admissible region method is generalized to define the PDF associated with a given admissible region. Using a Taylor series expansion, an analytical expression is derived which enables the generation of an approximate analytical model of the true PDF. This approximation is shown to be in good agreement with a numerically computed 'true' PDF. The methodology is extended to include multiple constraint hypotheses enabling a closed-form approximation of joint admissible region PDFs. The approach can also be applied to data association by computing the joint PDF from two statistically independent observations. The method presented improves initial orbit determination initialization with a single observation sequence by generating an initial PDF that correctly incorporates observation and assumed parameter uncertainties.

## V. Acknowledgments

This research is supported by the GEM Fellowship and AFOSR Contract #FA9550-13-1-0203.

## References


[1] L. C. G. Shepherd, "Space Surveillance Network," *Shared Space Situational Awareness Conference, Colorado Sprincs, CO*, 2006.

[2] R. A. Williamson, "Assuring the sustainability of space activities," *Space Policy*, Vol. 28, No. 3, 2012, pp. 154 – 160. Highlight: Assuring the sustainability of space activities, doi:10.1016/j.spacepol.2012.06.010.

[3] NASA, "Handbook for Limiting Orbital Debris," 2008.

[4] J. Siminski, O. Montenbruck, H. Fiedler, and T. Schildknecht, "Short-arc tracklet association for geostationary objects," *Advances in Space Research*, Vol. 53, No. 8, 2014, pp. 1184 – 1194, doi:10.1016/j.asr.2014.01.017.

[5] L. G. Taff, "On initial orbit determination," *Astronomical Journal*, Vol. 89, Sept. 1984, pp. 1426–1428, doi:10.1086/113644.

[6] P. Seitzer, R. Smith, J. Africano, K. Jorgensen, E. Stansbery, and D. Monet, "MODEST observations of space debris at geosynchronous orbit," *Advances in Space Research*, Vol. 34, No. 5, 2004, pp. 1139 – 1142. Space Debris, doi:10.1016/j.asr.2003.12.009.

[7] A. Milani, G. F. Gronchi, M. d. Vitturi, and Z. Knežević, "Orbit determination with very short arcs. I admissible regions," *Celestial Mechanics and Dynamical Astronomy*, Vol. 90, No. 1-2, 2004, pp. 57–85, doi:10.1007/s10569-004-6593-5.

[8] M. J. Holzinger, "Initial Orbit Determination, Data Association, and Admissible Regions of Space Objects using Magnetometers," *Journal of Guidance, Control, and Dynamics (accepted in April, 2014)*, 2014.

[9] A. Milani, G. F. Gronchi, Z. Kneevi, M. E. Sansaturio, and O. Arratia, "Orbit determination with very short arcs: II. Identifications," *Icarus*, Vol. 179, No. 2, 2005, pp. 350 – 374, doi:10.1016/j.icarus.2005.07.004.

[10] G. Tommei, A. Milani, and A. Rossi, "Orbit determination of space debris: admissible regions," *Celestial Mechanics and Dynamical Astronomy*, Vol. 97, No. 4, 2007, pp. 289–304, doi:10.1007/s10569-007-9065-x.

[11] K. Fujimoto and D. J. Scheeres, "Applications of the admissible region to space-based observations," *Advances in Space Research*, Vol. 52, No. 4, 2013, pp. 696 – 704, http://dx.doi.org/10.1016/j.asr.2013.04.020.

[12] D. Farnocchia, G. Tommei, A. Milani, and A. Rossi, "Innovative methods of correlation and orbit determination for space debris," *Celestial Mechanics and Dynamical Astronomy*, Vol. 107, No. 1-2, 2010, pp. 169–185, doi:10.1007/s10569-010-9274-6.

[13] K. Fujimoto, D. J. Scheeres, J. Herzog, and T. Schildknecht, "Association of optical tracklets from a geosynchronous belt survey via the direct Bayesian admissible region approach," *Advances in Space Research*, Vol. 53, No. 2, 2014, pp. 295 – 308, doi:10.1016/j.asr.2013.11.021.

[14] K. Fujimoto, J. Maruskin, and D. Scheeres, "Circular and zero-inclination solutions for optical observations of Earth-orbiting objects," *Celestial Mechanics and Dynamical Astronomy*, Vol. 106, No. 2, 2010, pp. 157–182, doi:10.1007/s10569-009-9245-y.

[15] J. M. Maruskin, D. J. Scheeres, and K. T. Alfriend, "Correlation of Optical Observations of Objects in Earth Orbit," *Journal of Guidance, Control, and Dynamics*, Vol. 32, No. 1, 2009, pp. 194–209, doi:10.2514/1.36398.

[16] K. DeMars, M. Jah, and P. Schumacher, "Initial Orbit Determination using Short-Arc Angle and Angle Rate Data," *Aerospace and Electronic Systems, IEEE Transactions on*, Vol. 48, No. 3, 2012, pp. 2628–2637, doi:10.1109/TAES.2012.6237613.

[17] K. DeMars and M. K. Jah, "Probabilistic Initial Orbit Determination Using Gaussian Mixture Models," *Journal of Guidance Control, and Dynamics*, Vol. 36, No. 5, 2013, pp. 1324–1335, doi:10.2514/1.59844.

[18] R. M. Weisman and M. K. Jah, "Uncertainty Quantification for Angles-Only Initial Orbit Determination," *AAS/AIAA Spaceflight Mechanics Meeting, Santa Fe, AAS 14-434, January 2014*, 2014.

[19] J. A. Vickers, "How Surfaces Intersect in Space: An Introduction to Topology (2nd edn)," *Classical and Quantum Gravity*, Vol. 13, No. 12, 1996, doi:10.1088/0264-9381/13/12/021.

[20] A. Milani, G. Gronchi, M. Vitturi, and Z. Kneevi, "Orbit determination with very short arcs. I admissible regions," *Celestial Mechanics and Dynamical Astronomy*, Vol. 90, No. 1-2, 2004, pp. 57–85, doi:10.1007/s10569-004-6593-5.

[21] S. Kullback and R. A. Leibler, "On Information and Sufficiency," *The Annals of Mathematical Statistics*, Vol. 22, 03 1951, pp. 79–86, doi:10.1214/aoms/1177729694.